sustainability

MDPI

Article

Simulations of Wind Formation in Idealised Mountain–Valley Systems Using OpenFOAM

Santiago Arias, Jose I. Rojas *, Rathan B. Athota and Adeline Montlaur

Department of Physics, Division of Aerospace Engineering, Universitat Politécnica de Catalunya, c/ Esteve Terradas, 7, 08860 Castelldefels, Spain

* Correspondence: josep.ignasi.rojas@upc.edu; Tel.: +34-93-413-4130

Abstract: An OpenFOAM computational fluid dynamics model setup is proposed for simulating thermally driven winds in mountain–valley systems. As a first step, the choice of Reynolds Averaged Navier–Stokes $k-\varepsilon$ turbulence model is validated on a 3D geometry by comparing its results vs. large-eddy simulations reported in the literature. Then, a numerical model of an idealised 2D mountain–valley system with mountain slope angle of 20° is developed to simulate thermally driven winds. A couple of top surface boundary conditions (BC) and various combinations of temperature initial conditions (IC) are tested. A transient solver for buoyant, turbulent flow of incompressible fluids is used. Contrary to classical approaches where buoyancy is set as a variable of the problem, here temperature linearly dependent with altitude is imposed as BC on the slope and successfully leads to thermally driven wind generation. The minimum fluid domain height needed to properly simulate the thermally driven winds and the effects of the different setups on the results are discussed. Slip wall BC on the top surface of the fluid domain and uniform temperature IC are found to be the most adequate choices. Finally, valleys with different widths are simulated to see how the mountain–valley geometry affects the flow behaviour, both for anabatic (daytime, up-slope) and katabatic (nighttime, down-slope) winds. The simulations correctly reproduce the acceleration and deceleration of the flow along the slope. Increasing the valley width does not significantly affect the magnitude of the thermally driven wind but does produce a displacement of the generated convective cell.

Keywords: slope; thermally driven winds; mountain–valley; anabatic; katabatic; computational fluid dynamics (CFD); OpenFOAM

Citation: Arias, S.; Rojas, J.I.; Athota, R.B.; Montlaur, A. Simulations of Wind Formation in Idealised Mountain–Valley Systems Using OpenFOAM. *Sustainability* **2023**, *15*, 1387. https://doi.org/10.3390/su15021387

Academic Editor: Mohamed A. Mohamed

Received: 28 September 2022
Revised: 14 December 2022
Accepted: 4 January 2023
Published: 11 January 2023

1. Introduction

Thermally driven winds appear in mountainous areas and valleys due to buoyancy effects caused by the temperature gradients associated with the diurnal heating–cooling cycle of the lower atmosphere. These winds develop persistently over complex topographies of multiple scales [1] and reverse their direction twice a day. During daytime, winds may flow up-valley from the plain to the mountain massif or up-slope (the so-called anabatic winds: upward warm flows along slopes). Conversely, during nighttime, winds may flow down-valley from the mountain massif to the plain or down-slope (the so-called katabatic winds: downward cold flows along slopes).

Since Prandtl [2] proposed his classic model for viscous fluid flows along uniformly cooled/heated infinite slopes in stably stratified environments, exact within the Boussinesq framework, many proposals have been made to extend it, e.g., to include Coriolis effects [3,4], time-dependency [5], spatially varying eddy viscosity and diffusivity [6], variations in the surface forcing [7], effects of changing slope angle [8], etc. Similarly, many works have analysed the effect on thermally driven winds of a variety of factors (e.g., the slope angle or the temperature difference between the atmosphere and mountain slopes) or have studied thermally driven winds in more complex configurations [9], whereas Prandtl's model is only applicable sufficiently far from ridges and valleys [5]. For

example, Egger [10] proposed an analytical model for thermally induced valley winds and conducted numerical studies of mountain–valley flows in 2D and 3D domains also using the Boussinesq approach. More recently, the interactions of slope flows with valley systems have also been investigated in 2D and 3D using large-eddy simulations (LES) [11]. Indeed, both LES [12–16] and direct numerical simulations (DNS) [1,17] have been used to study thermally driven winds and slope flows with high realism but generally over simple geometries, as these simulations involve high computational cost. More recently, new strategies such as stochastic modeling have gained much attention in the analysis of weather, climate, and ABL flows [18–23].

Similarly, dedicated numerical codes and commercial computational fluid dynamics (CFD) software have been used for wind resource assessment in complex terrains [24] and for studying thermal flows, e.g., using Alya High Performance Computing (HPC) multi-physics parallel solver [25], including in urban environments, e.g., using ANSYS-Fluent CFD [26], as previous works have shown that thermally driven winds can reach relatively high speeds [27,28]. Moreover, these winds show higher regularity and periodicity than synoptic winds [27,29] and thus can be more predictable. This is of special interest to the current energy market, since a critical issue is matching the energy demand with the renewable energy production [30].

Although LES and DNS could overcome some of the limitations of the previous CFD analyses, they are not so suitable for practical applications due to their high computational cost. To overcome this drawback, the use of Reynolds-Averaged Navier–Stokes (RANS) and detached-eddy simulations (DES) [31] appears to be key. In this regard, OpenFOAM v1712 is used in the present research. OpenFOAM is a free open-source software licensed under the General Public License, which has already been used to simulate flows over complex terrains, urban areas, etc. [32–34] and to compute the atmospheric boundary layer (ABL) over flat or complex terrain using LES [35,36]. To the best of our knowledge, little research has been published on the use of OpenFOAM for simulating thermally driven winds. Very recently, Cintolesi et al. [37] simulated an anabatic flow in a simplified geometry consisting of a uniformly heated double slope in an isothermal water tank using LES. The development of OpenFOAM numerical models for helping investigate these winds, which is precisely the main objective of this work, is thus of high interest, e.g., for wind-energy applications and for providing further insight on the structure and properties of these ABL flows.

Particularly, in this research, an OpenFOAM numerical model for simulating slope winds in a simple mountain–valley system has been set up and tested. First, a 3D model is checked against LES results in the literature to find the most appropriate RANS turbulence model. Then, we investigate, in a 2D computational domain, the performances of a couple of top surface boundary conditions (wall or symmetry) and various combinations of temperature and pressure initial conditions (uniform or altitude-dependent fields). It is worth noting that, unlike other typical works on slope winds [17,38] where buoyancy is set as a variable of the problem, temperature is used here to allow more straightforward tuning in applied problems, such as in wind resource assessment, where temperature data can be easily available. Once a most suitable set of boundary and initial conditions is established, the minimal fluid domain height for our purposes is validated. Finally, the effects of the valley width on the flow behaviour are studied. The 2D problem studied here, aside from being significantly less expensive computationally, is still very interesting as earlier works have revealed that katabatic winds may be reasonably considered as 2D in several areas of the world, such as in vast portions of Antarctica [39,40].

Following this introduction, Section 2 presents the methodology used in this research, while Section 3 shows the validation of the numerical model, and Section 4 presents the results and discussion. Finally, the main findings and conclusions of this research are summarised in Section 5.

2. Materials and Methods

2.1. Governing Equations and Main Assumptions

If the flow field is assumed to be a continuum (i.e., the fluid properties are continuous in both space and time), then, the mass, momentum, and energy conservation equations (Navier–Stokes equations) can be used to describe the flow behaviour Thermally driven winds are considered to be due to natural convection, and the formation of the ABL is driven by temperature gradients, while in forced convection it is driven by external pressure gradients. Thus, in our problem, the energy and momentum conservation equations are coupled, and unless information from the energy equation goes into the momentum equation, we cannot solve for the ABL growth. This can be overcome using the Navier–Stokes equations with Boussinesq approximation. In the latter, if heat transfer is non-negligible, then the flow properties usually depend on temperature. Furthermore, if the variation of density ρ is not significant, ρ can be considered constant in the unsteady and convection terms, but not in the body force term of the Navier–Stokes equations (i.e., density differences are ignored except where they appear in terms multiplied by the gravitational acceleration vector $\vec{g}$) [38].

In this research, we used the Boussinesq approximation, as in [10,38,41], and these assumptions: the air is considered as Newtonian and a dry perfect gas at rest [16]; the slope angle and eddy viscosity and diffusivity coefficients are treated as constants, as in [41]; radiation and Coriolis effects are negligible, since we focus on relatively small scales and local mechanisms in the near-ground-surface region [1,16,38]; and the geostrophic wind velocity is zero; and the diffusion is predominant in the slope-normal direction compared to along the slope. Following these hypotheses, the governing equations are:

$$\nabla \cdot \vec{U} = 0 \tag{1}$$

$$\frac{\partial \vec{U}}{\partial t} + \nabla \cdot (\vec{U}\vec{U}) - \nabla \cdot (2\nu_{eff} D(\vec{U})) = -\frac{1}{\rho_0}(\nabla p - \rho\vec{g}) \tag{2}$$

$$\frac{\partial T}{\partial t} + \nabla \cdot (\vec{U}T) - \nabla \cdot \alpha_{eff} \nabla T = 0 \tag{3}$$

where $\vec{U}$ is the velocity vector, t the time, ν_{eff} the effective kinematic viscosity (sum of molecular kinematic viscosity ν and kinematic turbulent viscosity ν_t), $D(\vec{U}) = \frac{1}{2}\left(\nabla\vec{U} + (\nabla\vec{U})^T\right)$ the strain rate tensor, p the static pressure, T the temperature, ρ_0 the reference density at the reference temperature T_0, and α_{eff} the effective thermal diffusivity. The density is updated in the temperature governing equation using the Boussinesq approximation:

$$\rho = \rho_0(1 - \beta(T - T_0)) \tag{4}$$

where β is the thermal volume expansion coefficient (set as a constant here), while α_{eff} is:

$$\alpha_{eff} = \frac{\nu}{Pr} + \frac{\nu_t}{Pr_t} \tag{5}$$

where Pr and Pr_t are the Prantl and turbulent Prantl numbers.

2.2. Solver Settings

OpenFOAM v1712 features several solvers based on finite volume methods for solving the governing equations of diverse fluid problems, including the necessary heat transfer analysis for studying thermally driven winds, as well as various turbulence and wall function models. The latter account for surface roughness effects, providing a turbulent kinematic viscosity boundary condition based on the turbulence kinetic energy (TKE). Among the various OpenFOAM solvers for heat transfer analysis that could a priori seem applicable for studying the behaviour of thermally driven winds, the steady-state (*buoyantBoussinesqSimpleFoam*) and transient (*buoyantBoussinesqPimpleFoam*) solvers for

buoyant, turbulent flow of incompressible fluids were chosen. These use Navier–Stokes equations with Boussinesq approximation.

In this work, the simulations were performed with null roughness height (except for the comparative study in Section 3) and using a no-slip wall condition on the slope for the velocity boundary condition. To improve the stability of the simulation and to obtain better initial values for the flow velocity $\vec{U}$, turbulence kinetic energy k, thermal diffusivity α_{eff}, and turbulent kinematic viscosity ν_t, simulations were started with the steady-state solver until the residuals of all variables were below 10^{-3}. At this point, a sufficiently satisfactory initialisation of the simulations was reached, and they were thus switched to the transient solver.

Table 1 sums up the main numerical schemes used for both solvers for terms such as the derivatives in Equations (1)–(3). In particular, for the time-derivative terms, after the steady-state initialisation, a first-order *Euler* scheme was used. Once the simulations reached a stable mode (i.e., once the initial oscillations were damped, which was determined when the value of the along slope velocity at 5 m did not show changes of more than 1% during 1000 s), a second-order *Crank–Nicolson* scheme was set to improve the accuracy of the final results.

Table 1. Finite volume schemes used for OpenFOAM numerical simulations in this work.

Scheme Labels	Terms	Scheme Types	Accuracy Orders
ddtScheme	Time-derivative terms	*Euler*	1st order, implicit robust, bounded
		Crank-Nicolson	2nd order, implicit bounded
gradSchemes	Gradient terms	*Gauss linear*	2nd order
divSchemes	Convection terms, e.g., $\nabla \cdot U$	*Gauss upwind*	1st order, robust
		Gauss linear	2nd order
	Diffusion terms, e.g., $\nabla \cdot \nu(\nabla U)^T$	*Gauss linear*	2nd order
laplacianSchemes	Diffusion terms, e.g., $\nabla \cdot \kappa(\nabla T)$	*Gauss linear corrected*	2nd order

The *Gauss upwind* scheme was used initially for the convection terms. After initialisation, these terms were switched to a *Gauss linear* scheme, which was also used for the diffusion terms and gradient terms. Laplacian terms were evaluated through surface-normal gradients. These, evaluated at a cell face, are the components normal to the face at the centres of the two cells that the face connects [42]. This calculation is second-order accurate if the vector connecting the cell centres is orthogonal to the face, i.e., if they are at right-angles. This would be the orthogonal scheme, which requires a regular mesh, typically aligned with the Cartesian coordinate system. When perfect orthogonality cannot be obtained, to maintain second-order accuracy, an explicit non-orthogonal correction can be added to the orthogonal component, known as the corrected scheme. Given that the mesh used in this work has maximum non-orthogonality of 20°, which is above the maximum non-orthogonality accepted for the uncorrected scheme (5°), a *Gauss linear corrected* scheme was used. It includes an under-relaxation factor expressed as $\cos^{-1}(\alpha_g)$, where α_g is the angle between the vector normal to the face and the vector connecting the two cell centres. The correction increases in size as the non-orthogonality (i.e., the angle α_g) increases.

The OpenFOAM equation solvers, tolerances, and algorithms used in this work are summarised in Table 2. For instance, to solve for pressure (symmetric matrix), a pre-conditioned conjugate gradient (PCG) solver with diagonal incomplete-Cholesky (DIC) pre-conditioner was used. For other parameters such as velocity, temperature, turbulence dissipation rate ε, and TKE, a stabilised preconditioned (bi-) conjugate gradient (PBiCGStab) solver with diagonal incomplete-LU (DILU) pre-conditioner was used. Under-relaxation

factors were used for both the steady- and transient-state simulations (see Table 2), such that accurate flow variables are obtained for each time step with a stable mode of simulation.

Table 2. Solver settings used for OpenFOAM numerical simulations in this work.

Fluid Properties	Solver Settings	Choice
p	Solver	PCG
	Pre-conditioner	DIC
	Tolerance	10^{-6}
	Relaxation factor	0.3 in steady state
		1 in transient state
$\vec{U}$, T, ε, TKE	Solver	PBiCGStab
	Pre-conditioner	DILU
	Tolerance	10^{-6}
	Relaxation factor	0.7 in steady state
		1 in transient state

OpenFOAM can use different algorithms to couple, in an iterative procedure, the momentum and energy conservation equations; namely, the Semi-Implicit Method for Pressure-Linked Equations (SIMPLE), the Pressure Implicit with Splitting of Operator (PISO), and PIMPLE, which includes both PISO and SIMPLE. SIMPLE is the algorithm used for steady-state problems, and PISO and PIMPLE are used for transient problems (see [42] for more details). Since PIMPLE exhibits the features of both SIMPLE and PISO, in this work, for the sake of a better accuracy, PIMPLE was chosen over PISO. A Courant number of 0.07 was used because for solving ABL flow problems this number must be lower than 1.0, and, for better stability, it should be lower than 0.25 [43] (see Section 4.4 for an in-depth analysis of the time-step sensibility). In this work, the settings were such that the pressure and momentum equations were solved twice within each time step. Moreover, it was chosen to update the explicit non-orthogonal correction to the *Laplacian term*. In PIMPLE, the entire system of equations was set to loop for 6 times within each time step (through the *nNonOrthogonalCorrectors* parameter), as this led to satisfactory stability of our simulation results. Finally, the momentum-predictor method was switched on.

2.3. Turbulence Modelling

Capturing the wind velocity profile and flow structures near the slope surface correctly depends significantly on the near-surface models. Namely, in [44], the best performance was provided by a RANS/LES hybrid eddy viscosity model. As per turbulence models in OpenFOAM aside from LES, we can use RANS turbulence closures based on linear and non-linear eddy viscosity models. We can also use Reynolds stress transport models, as well as DES, which relate to a hybrid RANS-LES approach to turbulence modelling aimed at alleviating the costly near-wall meshing requirements imposed by LES.

A complete study of the impact of the turbulence model on the generation of thermally driven winds is left out of the scope of this work, but two RANS models ($k-\varepsilon$ and Re-Normalisation Group (RNG) $k-\varepsilon$) are studied and compared in Section 3.2. Since turbulence models such as $k-\varepsilon$ are only valid where the turbulence is fully developed and do not perform well in areas close to the wall, one can either resolve the viscosity-affected region in all the mesh down to the wall, leading to very fine meshes and consequently to significant computational times, or use wall functions, which can model the near-wall region and thus bridge the inner region between the wall and the region of fully developed turbulence. Wall functions allow coarser meshes near the wall, but the first cell centre still needs to be placed in the log-law region to ensure the accuracy of the results [45]. Amongst the RANS models, previous studies showed that the RNG $k-\varepsilon$ turbulence model with standard wall function gave better agreement with experimental data, e.g., for combined wind and buoyancy-driven flow, than the standard $k-\varepsilon$ model [26,46]. However, it typically requires a finer near-wall mesh, which can be very demanding for complex

problems or 3D problems, whereas $k-\varepsilon$ remains a classical choice in multiple wind-related applications [25,47,48]. Both models are studied in Section 3.2 applying the *kqRWallFunction*, which provides a simple wrapper around the zero-gradient condition for the turbulent kinetic energy k, and *epsilonWallFunction*, which provides a wall function for the turbulent kinetic energy dissipation rate ε (see [49] for more details).

3. Case Study 1: 3D Slope-Only Model and Comparison with Literature

This section aims at selecting the turbulence model and the top boundary conditions by reproducing 3D simulations of up-flows on a rough slope from [12,14], chosen because they simulate equivalent atmospheric conditions and roughness parameters. They also have experimental measurements (though in different conditions) to compare their results with, and, to the authors' knowledge, there are not many suitable experimental results in the literature. Only a few experimental investigations exist, e.g., [50], and it is hardly feasible to replicate those test conditions in a simple numerical model like the one presented in this work. Moreover, a typical shortcoming in experiments is a lack of measurements at low heights (0.5–3 m) [51].

3.1. Geometry and Setup

For the abovementioned purpose, 3D simulations of up-flows on a rough slope (of 10°) were conducted, following the method described in Section 2. Figure 1 shows the geometry and boundary conditions used here, following the work by Axelsen and van Dop [14].

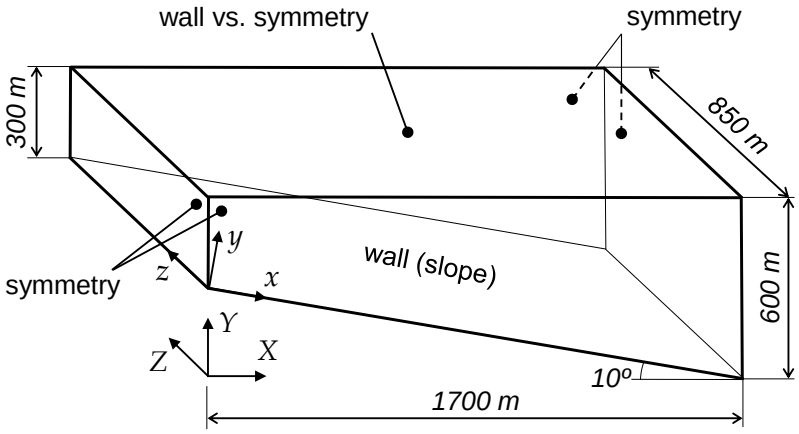

Figure 1. Geometry and setup for the 3D simulations.

Symmetric boundary conditions were applied to all vertical planes. On the slope, a no-slip wall boundary condition was applied, and a roughness height $z_0 = 0.2$ m was set, following [12,14]. All other numerical values for the constant parameters of the simulation were the ones used in [12] and correspond to realistic values for atmospheric cases. *kqRWallFunction* and *epsilonWallFunction* wall functions were imposed for k and ε, respectively. For the turbulent thermal diffusivity and the turbulent viscosity, *alphatJayatillekeWallFunction* (a wall function based on the Jayatilleke model, adequate for the Prandtl number considered here [52]) and *nutkWallFunction* (a wall constraint based on the turbulent kinetic energy) were used, respectively. On the top of the domain, two boundary conditions were tested: symmetry and slip wall. The flow was initially considered at rest. A rather coarse mesh of $128 \times 60 \times 64$ cells was generated, in order to match the mesh from [14].

3.2. Selection of the Turbulence Model

We tested both $k-\varepsilon$ and RNG $k-\varepsilon$ RANS turbulence models and compared the results with those of previous works [12,14], where simulations were performed with high-order convective schemes along with LES. Particularly, Schumann [12] used LES

with a second-order advection scheme, while Axelsen and van Dop [14] used LES with a sixth-order advection scheme.

Figure 2 shows the slope-normal profile of u_{avg}, i.e., the slope-normal height y vs. u_{avg}, which is computed by space averaging the along-slope velocity u over planes parallel to the mountain slope surface. It is important to note that these planes only cover 80% of the slope length along x to avoid lateral effects due to the symmetry boundary conditions.

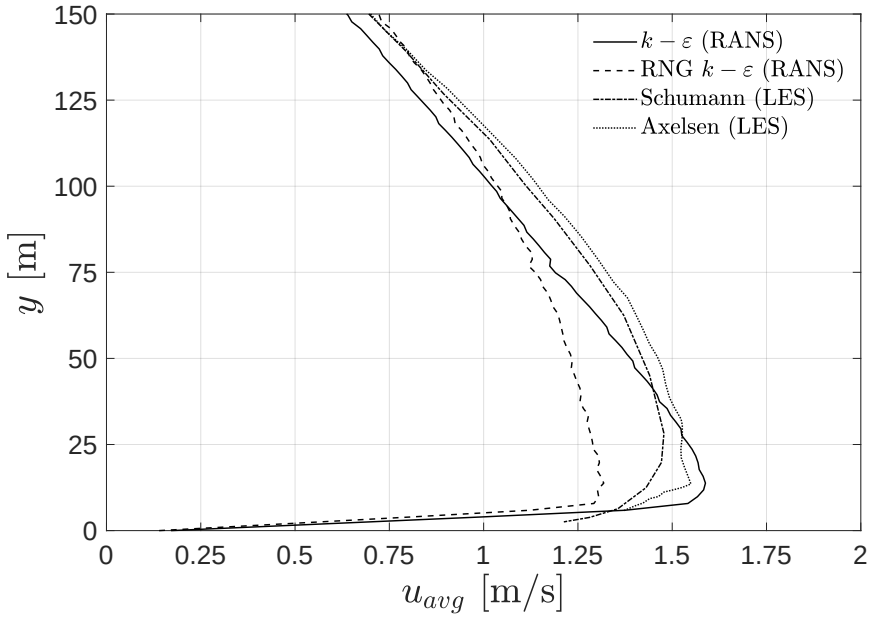

Figure 2. Comparison of y vs. u_{avg} from $k-\varepsilon$ and RNG $k-\varepsilon$ turbulence models against large-eddy simulations (LES) [12,14] for slip wall boundary condition on top surface.

For the $k-\varepsilon$ model, Figure 2 shows a maximum difference of 10.7% (7.4% at the peak) between our results and Schumann's [12], and a maximum difference of 11.9% (2.5% at the peak) with those from Axelsen and van Dop [14]. Table 3 summarises these differences. The RNG $k-\varepsilon$ turbulence model leads to maximum differences of, respectively, 13.9% and 16.5%, and under-predictions at the peak of 10.8% and 14.9%, thus,showing a worse agreement than the $k-\varepsilon$ model. When looking at the near-wall region (i.e., for y ranging from 0 to around 50 m), it was found in [14] that numerical models in general tend to predict a sharp wind peak compared to that obtained from in situ measurements. In this area, our numerical results show that RANS methods lead to sharper profiles (especially $k-\varepsilon$) than those obtained with LES (see Figure 2). This is likely due to the fact that RANS models underestimate the momentum mixing/transport at that height compared to LES.

Table 3. Error in the peak u_{avg} (ε_{peak}) and maximum error in u_{avg} ($|\varepsilon_{max}|$) when comparing the tested boundary conditions with LES results from Schumann [12] and Axelsen and van Dop [14].

	Turbulence	**Schumann**		**Axelsen and van Dop**	
Top BC	**Model**	ε_{peak} [%]	$\|\varepsilon_{max}\|$ [%]	ε_{peak} [%]	$\|\varepsilon_{max}\|$ [%]
Slip wall	$k-\varepsilon$	7.4	10.7	2.5	11.9
	RNG $k-\varepsilon$	−10.8	13.9	−14.9	16.5
Symmetry	$k-\varepsilon$	4.9	30.8	0.1	32.5
	RNG $k-\varepsilon$	20.9	24.9	15.3	24.5

3.3. Selection of the Top Surface Boundary Condition

We now want to validate our choice of boundary condition (BC) for the top surface by checking the performance of free-slip wall BC, which can be imposed on the top surface

to avoid inflow/outflow through that surface [9,10,16], against symmetry BC used, for example, in [26].

Figure 3 shows that, when using top symmetry BC, the u_{avg} profile is much sharper and follows a linear behaviour outside the near-wall region both for $k-\varepsilon$ and RNG $k-\varepsilon$ models. In this case, while the results obtained with the RNG $k-\varepsilon$ model above $y = 50$ m are closer to the reference results from LES than those from the $k-\varepsilon$ model, they overestimate the peak by around 25%. As for the $k-\varepsilon$ model, the differences at the flow peak between our results and the LES results from [12] and from [14] are only 4.9% and 0.1%, respectively, but they are up to 30.8% and 32.5%, respectively, when considering the maximum values of the errors.

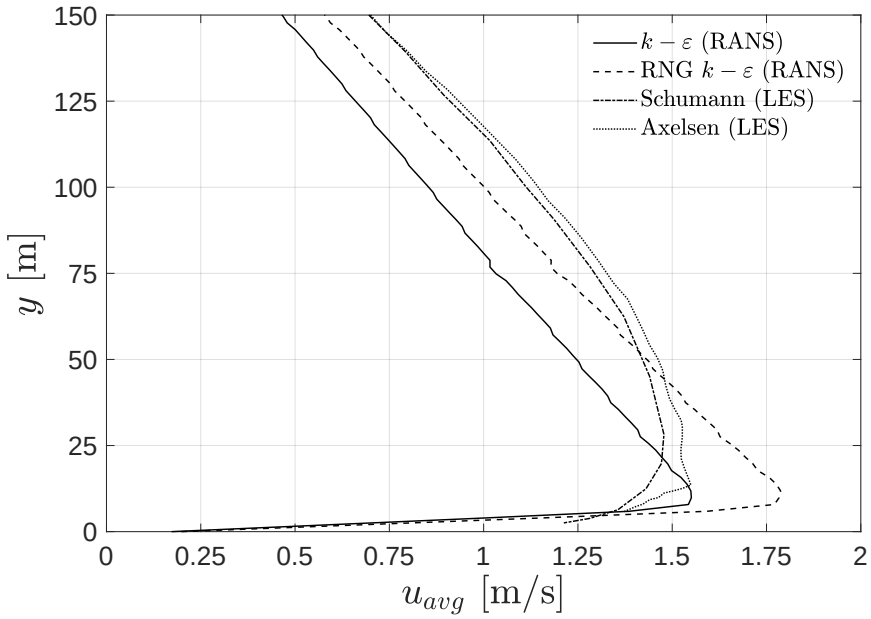

Figure 3. Comparison of y vs. u_{avg} from $k-\varepsilon$ and RNG $k-\varepsilon$ turbulence models against large-eddy simulations (LES) [12,14] for symmetry boundary condition on top surface.

To sum up, considering the results shown in Figures 2 and 3, our conclusion is that the $k-\varepsilon$ turbulence model with slip wall BC on the top surface is here the most convenient choice for performing the subsequent thermally driven wind simulations. A deeper study of the influence of the turbulence modelling (both RANS and LES) and a comparison with DNS is considered out of the scope of the current work but will be given special attention in future research. Once the turbulence model and this top BC have been selected, the next case study investigates several valley configurations. This study is conducted in 2D for computational cost restrictions.

4. Case Study 2: 2D Mountain–Valley Simulations

Building on our previous findings, the main objective of this case study is to simulate a buoyancy-driven flow due to the temperature difference between the mountain surface and the atmospheric field in a 2D mountain–valley configuration. Note that the setup for the simulations (e.g., the characteristic dimensionless numbers and models used in this case study) are the ones described in Sections 2.1 and 2.2, while the boundary and initial conditions are detailed hereafter.

4.1. Generation of the Studied Geometries

A simple geometry of a 2D mountain–valley system is used here, consisting of a domain including half of a mountain modelled with a slope of 20°, a height of 500 m along the Y-axis, a slope length of 1462 m along the x-axis, and a projected base width of 1374 m along the X-axis (see Figure 4). The fluid domain total width was set to 3022 m along the

X-axis, and thus the half of the valley included in the studied domain has a width W of 1648 m. Note that, from now on, and for the sake of simplicity, we use the term *valley width* to refer to W, although it is only the half-valley width. An initial computational height H of 2000 m along the Y-axis was set. The slope and height of the studied mountain roughly match the topography of places such as Los Angeles and Phoenix (USA), Tokyo (Japan), or Hong Kong (China), and slopes with angles used in recent investigations [1,11,38]. Moreover, the initial fluid domain dimensions were based on the orders of magnitude used in previous works [16,26]. Effects of the fluid domain height and the valley dimensions on the results are explained in Section 4.7 and Section 4.8, respectively.

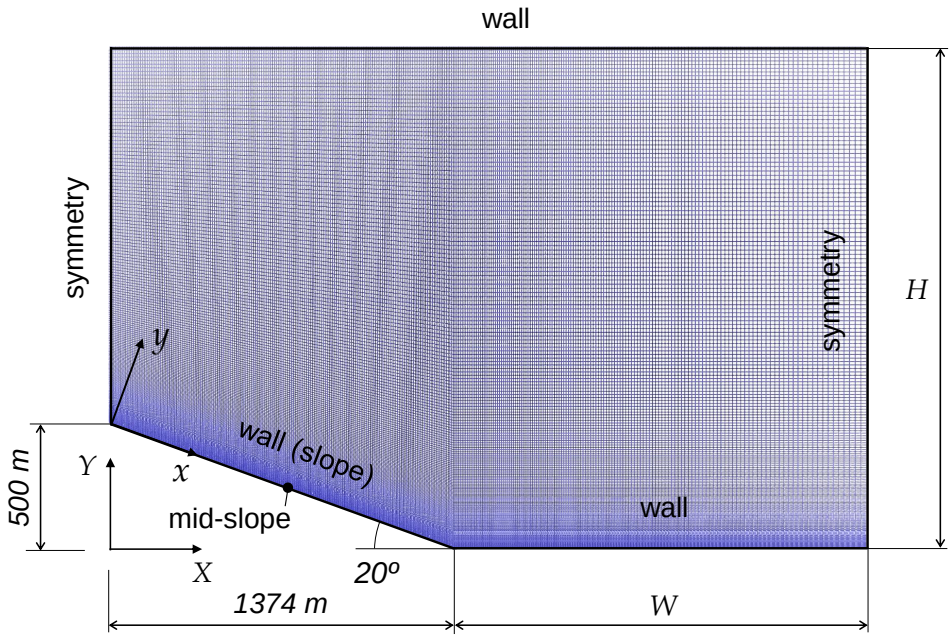

Figure 4. 2D mountain–valley geometry, mesh, and boundary conditions.

4.2. Boundary and Initial Conditions

Following OpenFOAM guidelines, though performing 2D simulations, a one-layer 3D mesh was built and empty boundary conditions were applied to its front and back surfaces. Symmetry boundary conditions were imposed on the left and right vertical surfaces to replicate a mountain–valley configuration in a mountain range. A free-slip wall boundary condition was imposed on the top surface as noted in Section 3.3.

A no-slip wall boundary condition was imposed on the slope and flat valley, as in [7,16,38]. There, *kqRWallFunction* and *epsilonWallFunction* wall functions were imposed for k and ε, *alphatJayatillekeWallFunction* for turbulent thermal diffusivity, and *nutkWallFunction* for turbulent viscosity. Zero-roughness height was considered in this case.

As for the temperature, the following profile was applied as the boundary condition on the slope and the flat surface of the domain:

$$T = T_0 + \Omega Y \tag{6}$$

where Ω is 4.5 K/km for the anabatic case and -4.5 K/km for the katabatic one, and $T_0 = 288.15$ K. Recall that the Y coordinate is in the opposite direction to gravity (while y is the slope-normal direction). Thus, while temperature varies with Y when we move up or down the slope, the valley has a constant temperature (as Y is constant) which does not change either as we move away from the slope. Particularly, it has the same temperature as the lowest point of the slope. Note that these boundary conditions in which temperature varies linearly along the slope are an innovative approach, following [7,53], where the surface buoyancy varies linearly down-slope.

The following settings were considered: $\beta = 1.05 \times 10^{-3}$ K^{-1}, $g = 9.81$ m/s^2, $\nu = 1.568 \times 10^{-5}$ m^2/s, $Pr = 0.9$, and $Pr_t = 0.7$. The resulting Reynolds, Grashof, and Rayleigh numbers characterising the physics of the fluid problem in our simulations are, respectively, $Re = 6.4 \times 10^5$, $Gr = 1.1 \times 10^{10}$, and $Ra = 8.7 \times 10^9$. These values of Gr and Ra are of the same order of magnitude as the values in, e.g., [1,16,37,54–56], so it can be considered that our problems are in the same fluid dynamics regimes.

As for initial conditions, since the flow experiences natural convection due to the temperature difference between the mountain slope and the atmosphere (fluid field), the wind speed was considered null as an initial condition, and no external pressure gradient was imposed [7]. Constant pressure was set as initial conditions, and two possibilities of initial conditions for the temperature are studied in Section 4.5. In the literature, similar CFD simulations have been performed with constant temperature imposed on the slope as a boundary condition and varying temperature in the atmospheric field as an initial condition [37,57]. Moreover, most works have used constant surface cooling/heating or flows forced using constant surface buoyancy flux, i.e., homogeneous surface forcing [1,17,38], while only a few have used inhomogeneous surface forcing, i.e., surface buoyancy or buoyancy flux that varies down-slope [7,41].

4.3. Validation of the Mesh

In this work, the *blockMesh* utility was used to generate the non-uniform structured mesh of the studied fluid domain by building the geometry as two blocks (one trapezoidal for the slope part and the other rectangular) as shown in Figure 4. In the originally chosen mesh, the vertical grid size starts at 0.089 m in the near-wall region, so the first vertical grid point of the mesh lies below the peak of the anabatic or katabatic jet [16] (examples of positions of the peak are given in Section 4.7). That size is also far below the 1.7 m used in [11] and the recommended minimum vertical mesh size of 1 m, necessary to accurately capture and resolve the large-scale shear of the wall jet developing along the slope [16]. This leads to a value of the non-dimensional wall distance y^+ of around 220, which is an adequate value for $k - \varepsilon$ RANS models. The maximum vertical cell size is 15 m, which is obtained near the top surface thanks to a constant expansion factor of 1.027 (1.02 was used in [16], reaching a vertical mesh size of 120 m in the top surface, at a height of 7.25 km). As per the horizontal grid spacing (which is usually much larger in these investigations [16], due to the typical behaviour of these flows), the along-slope size of the cells immediately over the slope is 6.5 m, growing up to 24.5 m at the rightmost end of the flat surface, leading to similar values as those found in the literature [16]. This leads to a mesh of 197,400 grid points and 98,072 hexahedral cells.

To validate the proposed mesh, a grid independence study was conducted for the vertical spacing by comparing the performance of the described mesh (197,400 grid points) with that of a finer (282,240) and a coarser mesh (148,292), for an anabatic simulation. Table 4 shows the maximum values of the along-slope flow velocity u_{max} at several points along the mountain slope, namely, at 40, 45, and 50% of the slope (starting from the slope base). Values of u_{max} are obtained for the three meshes, and their relative errors with respect to the finest mesh are shown. In this table and the following ones, all the values reported correspond to the end of the simulation. It can be seen that the error decreases from around 13% to 27% (coarsest mesh) to an acceptable value of around $\pm 2/3$% (proposed mesh).

Table 4. Results of maximum along-slope flow velocity u_{max} from the grid independence study at several positions along the slope, where 0% is the slope base and 100% the mountain apex.

	40% Slope		45% Slope		50% Slope	
Grid Points	u_{max} **[m/s]**	**Error [%]**	u_{max} **[m/s]**	**Error [%]**	u_{max} **[m/s]**	**Error [%]**
282,240	−0.240	-	−0.265	-	−0.291	-
197,400	−0.244	1.8	−0.259	−2.2	−0.283	−2.6
148,292	−0.304	26.7	−0.322	21.7	−0.328	12.7

It is also interesting to look at the obtained value of y^+ to further validate the chosen mesh. When using the $k-\varepsilon$ model along with standard wall functions, the y^+ values should be as in the latter case, and particularly between 30 and 500 [58,59]. In this work, y^+ ranges from 270 (coarsest mesh) to 160 (finest mesh), while for the proposed mesh y^+ is 220, which is in line with other similar studies [26]. Hence, it can be concluded that the originally proposed mesh with 197,400 grid points is satisfactory. Further refinement of the grid is not worth it since it substantially increases the computational cost while only leading to a small decrease in the obtained error (<3%).

4.4. Validation of the Time Step

Here, we study the effect of the time step on the numerical errors by selecting several time steps for the anabatic simulation. In all cases, the convergence condition by Courant–Friedrichs–Lewy (CFL) is satisfied; thus, all simulations converged satisfactorily. Table 5 shows the numerical errors of the results. As expected, once the CFL condition is met, the effect of Δt is limited, and $\Delta t = 0.008$ s is chosen for solving our unsteady flow problem since it leads to a level of error (0.6%) well below the mesh-related error observed in the mesh-independence study conducted in the previous section.

Table 5. Results of maximum along-slope flow velocity u_{max} from the time-step independence study.

Δt [s]	u_{max} [m/s]	Error [%]
0.006	−0.281	-
0.008	−0.283	0.6
0.010	−0.286	1.9

4.5. Selection of Temperature Initial Conditions

We now want to study the influence of the initial conditions (IC) on the thermally driven wind simulation results by comparing the results of imposing uniform vs. altitude-dependent temperature IC in the field. For the case of uniform temperature IC, we initially set $T_0 = 288.15$ K in the field, while if altitude-dependent temperature IC is considered, the temperature profile shown in Equation (6) is applied as IC in the field.

Figure 5 shows the time evolution of u_{5m}, which is the along-slope flow velocity at the mid-section of the mountain slope at 5 m in the slope-normal direction for several cases: constant and altitude-dependent temperature IC, for the anabatic and katabatic cases, while using a constant pressure IC. A better convergence of the simulation towards a steady state is obtained both for the anabatic and katabatic flows by setting constant temperature IC rather than using altitude-dependent IC. Figure 5b,d show that when using altitude-dependent temperature IC, even after 40,000 s of simulation, the flow has still not reached a steady state, whereas when using constant values as IC, the values of u_{5m} start reaching a steady value at around 10,000 s, as shown in Figure 5a,c.

We then analyse the convergence of the anabatic case more in-depth by studying the time evolution of $\varepsilon_{u_{max}}$ and $\varepsilon_{u_{5m}}$, i.e., the errors of u_{max} and u_{5m} at a given time, with respect to their final values, taken at t_∞ = 41,000 s, for the anabatic case with constant temperature IC in Figure 6. It can be seen that establishing an anabatic flow with an error lower than ≈1% takes around 25,000 to 30,000 s. Simulations were also conducted for the katabatic case, and the most interesting results are presented in Table 6. It can be seen that, overall, the settling time t_s (defined as the time to reach a velocity accuracy of 1% with respect to the value obtained at t_∞) for the katabatic simulations is quite shorter than for the anabatic ones. The explanation for this might be that simulations converge faster for katabatic flows because they are characterised by strong buoyancy damping of the turbulence, while anabatic flows are characterised by absolute static instabilities that induce convective motions above the heated slope [38].

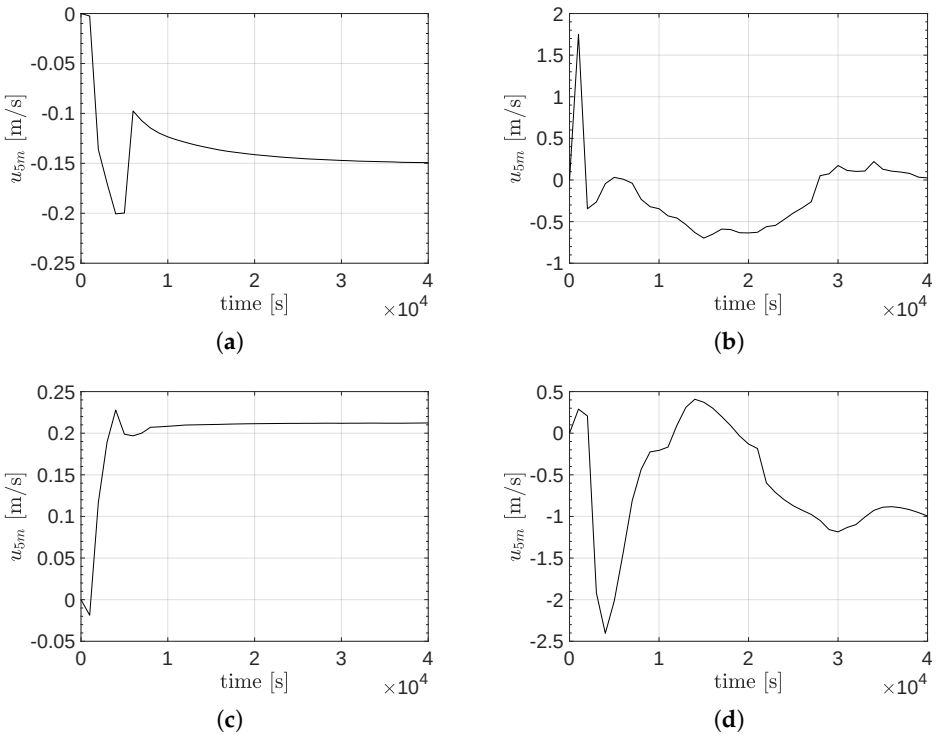

Figure 5. For the mid-slope position, along-slope velocity at a slope-normal distance of 5 m (u_{5m}) vs. time for uniform and altitude-dependent temperature initial condition (IC) for anabatic and katabatic cases: (**a**) anabatic: constant temperature IC; (**b**) anabatic: altitude-dependent temperature IC; (**c**) katabatic: constant temperature IC; (**d**) katabatic: altitude-dependent temperature IC.

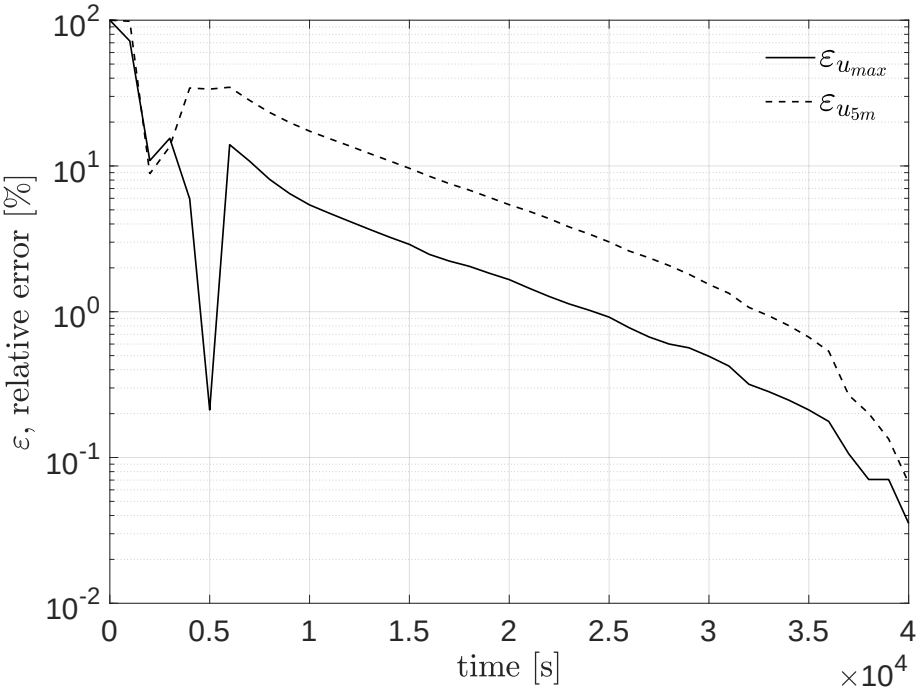

Figure 6. For the mid-slope position, $\varepsilon_{u_{max}}$ and $\varepsilon_{u_{5m}}$ (errors of u_{max} and u_{5m} with respect to their values at $t_\infty = 41{,}000$ s) vs. time for anabatic case with uniform temperature initial condition.

Table 6. Along-slope flow velocity at mid-slope and corresponding settling times t_s (times to reach 1% accuracy in the obtained velocity) for uniform temperature initial condition.

Flow Type	u_{max} [m/s]	$t_{s,max}$ [s]	u_{5m} [m/s]	$t_{s,5m}$ [s]
anabatic	−0.283	25,000	−0.149	33,000
katabatic	0.338	11,000	0.212	15,000

We conclude that setting the field temperature IC respecting space continuity with the slope temperature boundary condition decelerates the simulation convergence. Since the field eventually converges to a constant temperature, except for local changes in the near-slope region, imposing constant temperature IC is more efficient in terms of convergence and is thus set as such in all simulations.

4.6. Preliminary Results

The previous section showed that settling times were longer when simulating the anabatic case than when running the katabatic one (see Table 6). Figure 7 now shows the velocity contours and streamlines (close to the convective cell) for the anabatic and katabatic cases previously described. Vectors on top of the streamlines show the flow direction (clockwise and counter-clockwise vortices for the anabatic and katabatic cases, respectively). Note that far away from the slope, the velocity is very low, and the flow is practically at rest (dark blue colour). Recall that in all the velocity contour figures, the modulus of velocity ($U = |\vec{U}|$) is represented and that the scale maximum has been set to 0.1 m/s to facilitate visualisation of the lowest velocities, meaning that the dark red colour corresponds to flow velocities $\geq$ 0.09 m/s.

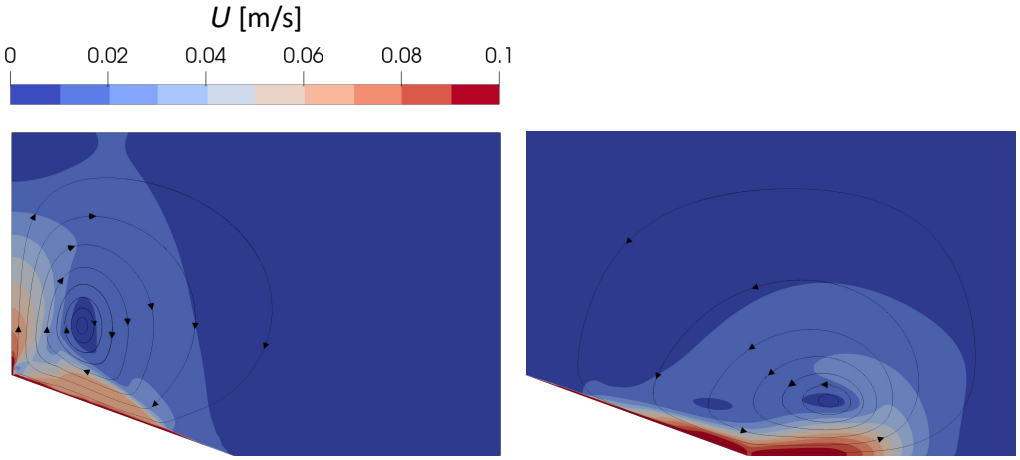

Figure 7. Velocity streamlines for anabatic (**left**) and katabatic (**right**) flows for a computational domain of total height $H = 2000$ m and valley width $W = 1648$ m (recall that the term "valley" refers to the flat bottom surface on the right-hand side).

Figures 8 and 9 show the along-slope velocity u and temperature T vs. the slope-normal distance y at different positions along the slope for the katabatic and anabatic flows, respectively. In both cases, the computational domain has total height $H = 2000$ m and valley width $W = 1648$ m. When studying the peak flow velocity, these slope-normal profiles of u exhibit qualitatively (and even quantitatively, if considering the relative variations) similar trends as the results reported in previous works. Namely, for the katabatic flow, the peak velocity increases as we move down the slope for the first half of the slope and then drops in the second half of the slope. Particularly, in [16], the peak velocity increases ≈34% from the point located at 71% to the point located at 54% from the slope base and drops by ≈65% from the point located at 54% to the point located at 40% from the slope base. In Figure 8, the peak velocity increases ≈30% from the point located at 70% to the point located at 50% from the slope base and drops by ≈40% from the point located at 50%

to the point located at 20% from the slope base. For the anabatic flow, the peak velocity increases monotonically as we move up the slope. Particularly, in [37], the peak velocity increases ≈38% from a point located at 33% to another point located at 50% from the slope base, while in Figure 9 the peak velocity increases ≈28% in the same slope segment.

As per the y-position of the peak velocity, in [16,37] it follows exactly the same trends observed for the peak velocity. For anabatic flow, it increases monotonically as we move up-slope, and for katabatic flow, it increases as we move down-slope for the first half of the slope, while it drops in the second half. In our anabatic case, though, the y-position of the peak velocity in the slope segment ranging from 35% to 50% from the slope base is constant. Thus, it does not match the trend reported in [37]. Nevertheless, for our katabatic case, it increases and then decreases, like in [16]. It can thus be concluded that these simulations reproduce the same flow acceleration and deceleration observed in the literature along the slope for both type of flows, while they reproduce the trend observed in the literature in the y-position of the peak velocity only for the katabatic case.

When looking at the vertical temperature profiles in Figures 8 and 9, a similar behaviour is distinguishable in general in all the positions along the slope. At $y = 0$ m, the temperature profile starts at the corresponding value of T as given by Equation (6). Then, as the slope-normal distance y increases, the temperature quickly tends to $T_0 = 288.15$ K. Thus, away from the slope, the temperature is mostly uniform in the whole fluid domain. As shown in Figures 8 and 9, the flow appears to behave as super-adiabatic, experiencing a large gradient of temperature very close to the slope surface, which produces a strong variation of T at very low heights, typically below 5 m.

As expected, the value of T at $y = 0$ m determines the temperature profile of each position along the slope. In this sense, Figure 8b shows how the temperature profiles are ordered correspondingly to their temperature at $y = 0$ m. According to Equation (6), the temperature in the slope decreases as the altitude increases for the katabasic case. For the positions along the slope shown in Figure 8b, the temperature at $y = 0$ m is equal to 287.7 (20%), 287.48 (30%), 287.25 (40%), and 287.03 K (50%). It can then be seen how in positions along the slope with higher temperature at $y = 0$ m, this also leads to higher temperatures when $y > 0$. Figure 8b also suggests that positions along the slope with smaller temperatures at $y = 0$ m produce smoother temperature profiles.

A similar behaviour can be seen in Figure 9 for the anabatic case. In this case, the temperature at $y = 0$ m is equal to 288.96 (35%), 289.07 (40%), 289.19 (45%), and 289.3 K (50%), increasing as the altitude increases, as given by Equation (6). Again, positions along the slope with higher temperature at $y = 0$ m lead to higher temperatures when $y > 0$. In the anabatic case, positions along the slope with higher temperatures at $y = 0$ m now produce smoother temperature profiles. In all cases, and though the differences between the temperature profiles are small, smoother vertical temperature profiles lead to higher peaks of along-slope velocity u (see for example the profiles at 50% of the slope in both Figures 8 and 9), which is a classical trend as reported in the literature [16,37,60].

These results confirm the local behaviour of these winds (i.e., the areas affected by slope flows are concentrated close to the slope) and suggest that the computational domain height may noticeably affect the generated convective cell. This is why the effect of the domain height and how it should properly selected is studied next in Section 4.7. It is also expected that geometric parameters of the mountain–valley configuration also affect the size and location of the vortices in Figure 7. This is why the effect of the valley width is studied in Section 4.8, while other parametric studies, such as analysing the effect of the slope angle, are left for future work.

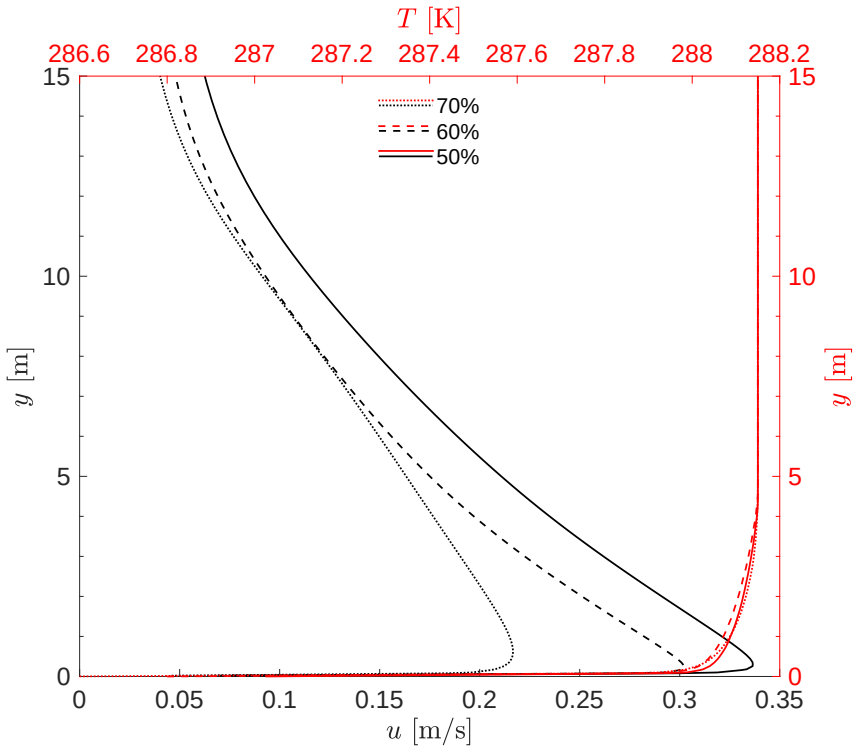

(**a**)

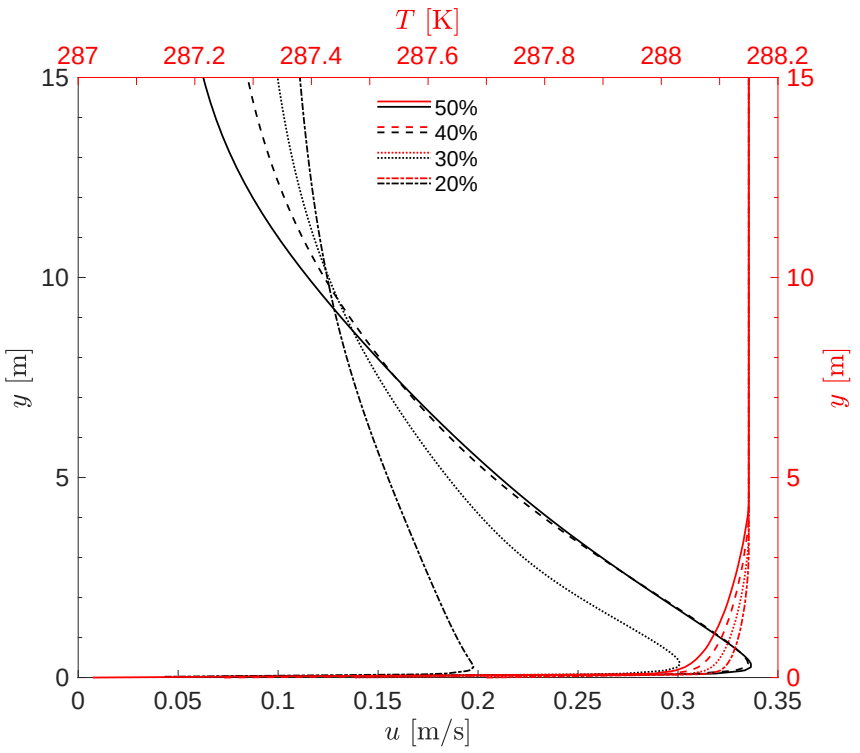

(**b**)

Figure 8. Katabatic flow: along-slope velocity u and temperature T vs. slope-normal distance y at different positions along the slope (indicated in % of the slope, starting from the slope base) for a computational domain of total height $H = 2000$ m and valley width $W = 1648$ m: (**a**) first half of the slope, considering the direction of the katabatic flow motion; (**b**) second half of the slope, considering the direction of the katabatic flow motion.

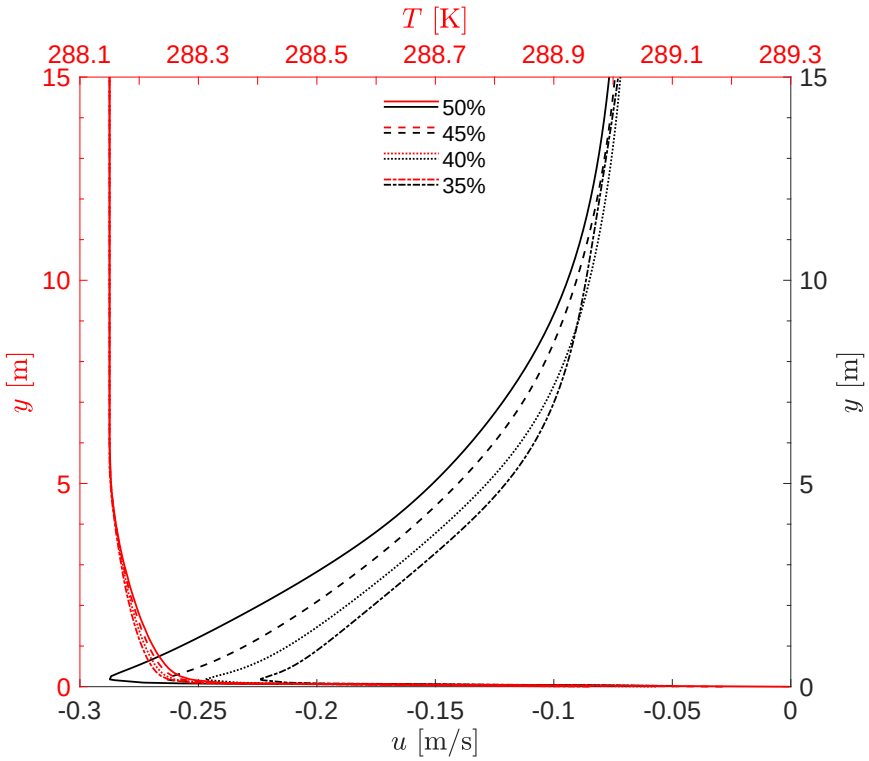

Figure 9. Anabatic flow: along-slope velocity u and temperature T vs. slope-normal distance y at different positions along the slope (indicated in % of the slope, starting from the slope base) for a computational domain of total height $H = 2000$ m and valley width $W = 1648$ m.

4.7. Effect and Selection of Fluid Domain Height

In this section, we aim to validate the minimum height of the fluid domain suitable for this research, following the domain-size convergence study conducted in [1]. The initial height of the fluid domain tested here ($H = 2000$ m) was based on the orders of magnitude of fluid domains used in previous works [11,12,14,16] and on the typical heights of thermally driven wind convective cells ranging from 50 to 500 m [29,61] (it can be assumed that all these studies refer to fluid dynamics regimes equivalent to ours because the orders of magnitude of all the parameters involved in the definitions of *Re*, *Gr*, and *Ra* are similar). Furthermore, since anabatic winds show the vortices that reach highest heights (see Figure 7) and thus can be more affected by the height of the top boundary of the domain, the height validation study conducted here is based on an anabatic configuration.

Along with the reference domain height ($H = 2000$ m), a smaller height ($H = 1400$ m), as well as two larger heights ($H = 2600$ and 3200 m), were tested in the frame of this validation. Figure 10 shows the generated wind for the four heights. For the sake of clarity, only the field over the slope is presented in these figures, as that is where the cell due to the anabatic wind develops. It can be clearly seen that $H = 1400$ m would be too small since the cell still shows non-null velocity on the top wall. Differences can still be clearly observed between the results obtained for $H = 2000$ m and for $H = 2600$ m. For instance, while the top of the cell gets close to the domain top when $H = 2000$ m, it has completely vanished at the domain top for the case $H = 2600$ m. The near-slope areas for these two cases also show some visible differences for the velocity magnitude of the field. Nevertheless, when observing the case with $H = 3200$ m, most differences vanish, and the velocity fields appear very similar both away and in the near-slope area.

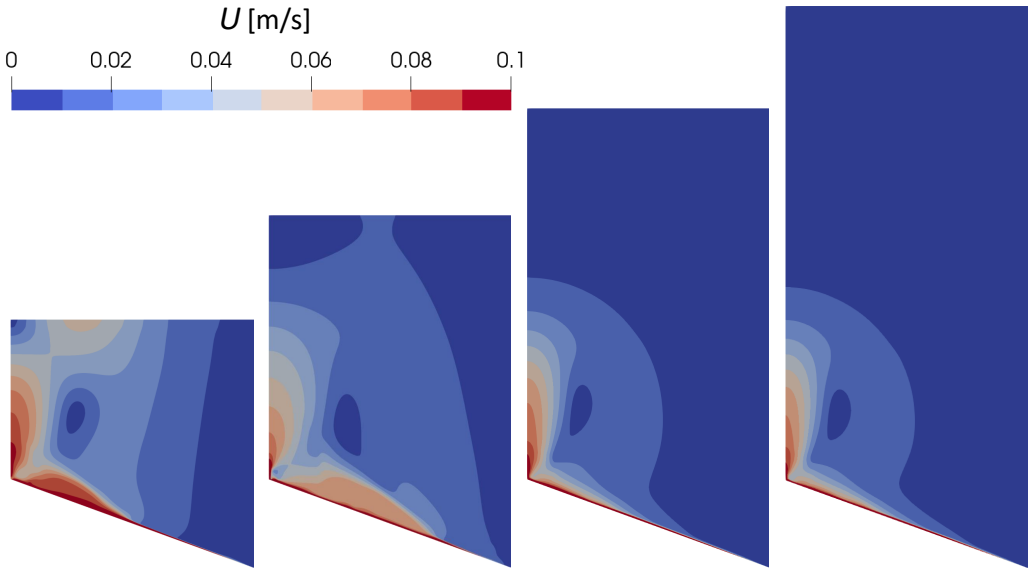

Figure 10. Anabatic flow: effect of domain height H on the velocity contours and cell generated over the slope (from left to right: $H = 1400$, 2000, 2600, and 3200 m) for valley width $W = 1648$ m (the part of the computational domain over the flat valley is not shown here since velocity is close to zero in this area).

To be able to better appreciate the differences in the results obtained for these four cases, Figure 11 shows how the domain height affects the up-slope velocity profile at mid-slope as a function of the slope-normal distance. It is clear that the smaller the domain height (e.g., $H = 1400$ m) is, the less the wind speed profile resembles logarithmic, and the more linear it seems. To a much lesser extent, the same behaviour is observed for $H = 2000$ m, and it is only for $H = 2600$ and 3200 m that the wind speed profile seems more logarithmic.

Table 7 gives more quantitative information on this validation study of the domain height; particularly, for the mid-slope position, it shows u_{max}, u_{5m}, and u_{10m}, as well as the slope-normal distance at which the velocity peak is located (y_{max}). It is evident that once the domain height is sufficiently large (i.e., above $H = 1400$ m), the differences in the numerical results for the peak velocity and peak position become smaller as we increase H. Indeed, the peak position remains constant from $H = 2000$ m and above, and though there are still numerical differences in the obtained along-slope velocities, we believe that the small improvements in the accuracy of the results do not justify the much higher computational cost. After this study, it is confirmed that, as observed in [1], once the domain height is sufficiently large, the variations of statistics are negligible, and, from now on, $H = 2600$ m is taken as the selected domain height.

4.8. Effect of Valley Width

In this section, the influence of the valley width W (see Figure 4) on the flow behaviour is studied both for anabatic and katabatic cases, using the validated domain height $H = 2600$ m. Note that while the previous analysis of the effect of the domain height was indeed a domain-height selection study (that is, a study aimed at identifying the necessary height of the fluid domain so that the behaviour of the anabatic flow over the slope was not affected by the domain height), the analysis conducted here for different valley widths is intended to ascertain the impact of the valley width on slope winds in general, from the physical mechanism point of view. For this purpose, the results obtained for the reference computational domain with $W = 1648$ m are compared to those obtained for two additional mountain–valley configurations with different values of W. Taking the semi-mountain base (with width 1374 m) as a reference, we considered a valley width three times shorter ($W = 458$ m) and a valley width three times longer ($W = 4122$ m).

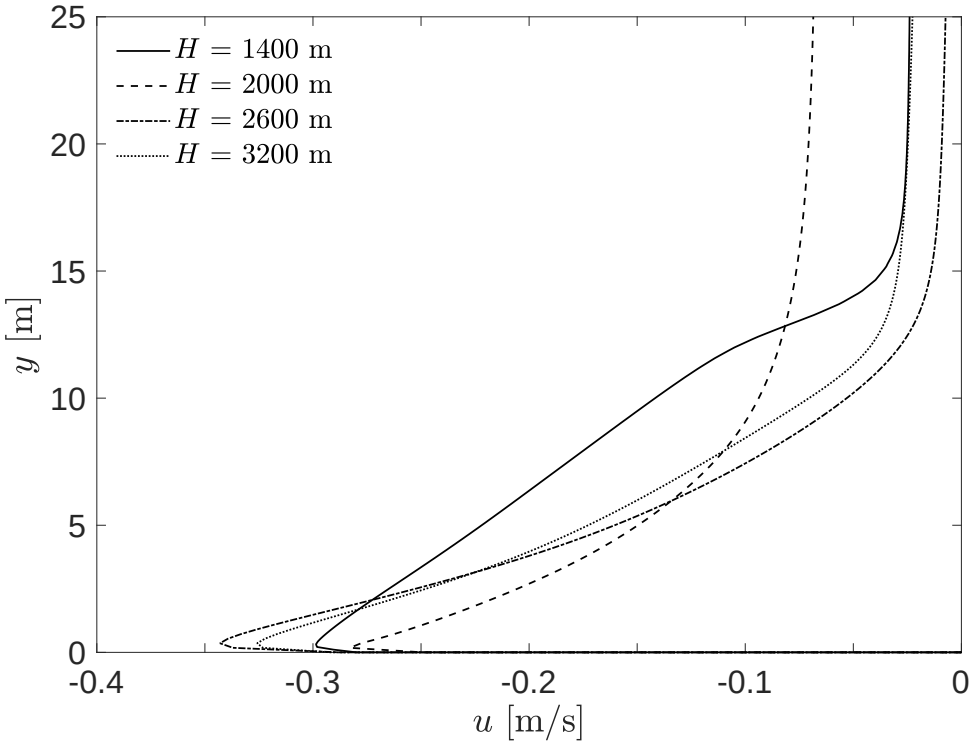

Figure 11. Anabatic flow: effect of domain height H on the along-slope velocity u vs. slope-normal distance y profile at mid-slope position for valley width $W = 1648$ m.

Table 7. For the mid-slope position, maximum along-slope velocity (u_{max}) and along-slope velocity at a slope-normal distance of 5 m (u_{5m}) and 10 m (u_{10m}) for valley width $W = 1648$ m and different domain heights H.

Parameter	$H = 1400$ m	$H = 2000$ m	$H = 2600$ m	$H = 3200$ m
u_{max} [m/s]	−0.299	−0.283	−0.346	−0.326
u_{5m} [m/s]	−0.220	−0.150	−0.167	−0.172
u_{10m} [m/s]	−0.140	−0.094	−0.062	−0.070
y_{max} [m]	0.318	0.179	0.359	0.359

Starting with the anabatic configuration, Figure 12 shows the velocity contours obtained for the various tested valley widths. Bear in mind that for clarity purposes, the field over the flat valley is not represented in these figures because for the tested cases the flow velocity is virtually null in this region.

It is observed that a narrower valley leads to much higher vertical velocity on the left-hand side symmetry boundary condition, while the effect on the flow over the slope and close to it is much more limited. Assuming that the vertical motions at the boundary are a result of flow convergence and thus directly related to the mass flux in the slope-flow layer, higher vertical motions for the narrower model domains would mean a higher mass flux in these simulations. This can actually be seen in Figure 13, which, to facilitate a better appreciation of the differences obtained, shows the velocity profiles for the three studied geometries from which it is evident that a narrower valley leads to a more linear profile with a slightly lower absolute value of u_{max}.

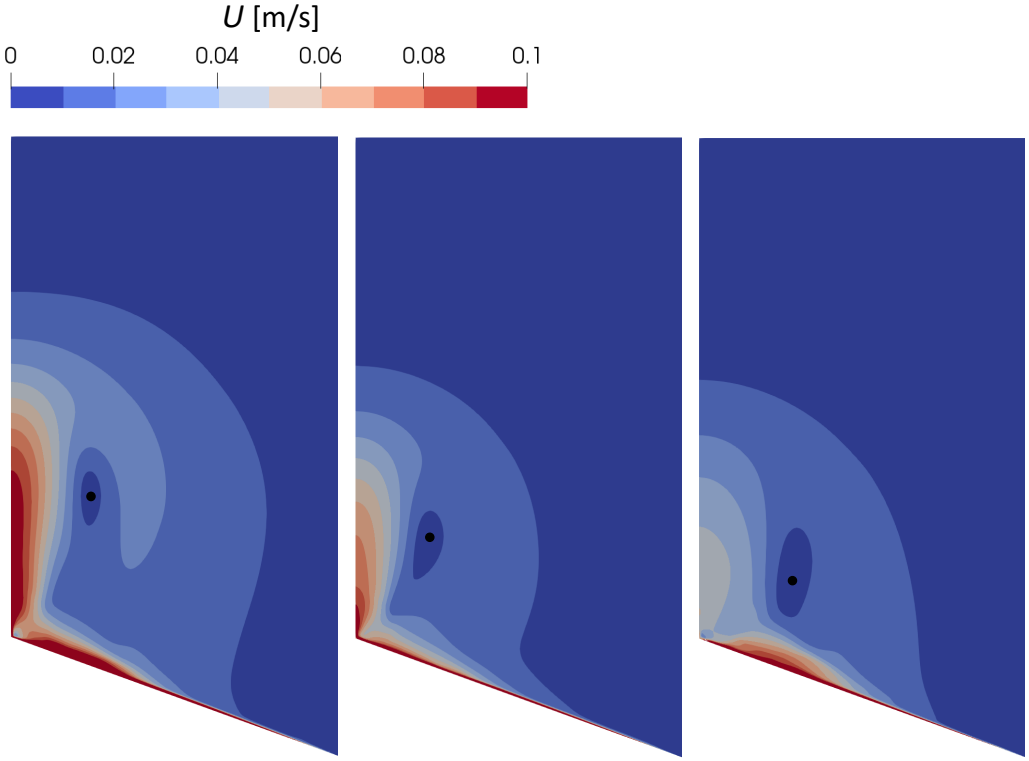

Figure 12. Anabatic flow: effect of valley width W on the velocity contours and cell generated over the slope (from left to right: W = 458, 1648, and 4122 m) for domain height H = 2600 m (the fluid domain over the flat valley is not shown here since velocity is close to zero in this area). The convective cell centre is indicated with a black dot.

Once the valley reaches a sufficiently large width, the width does not affect the velocity profile at mid-slope much, e.g., the peak of the velocity profile remains approximately the same. This trend can be confirmed in Table 8, showing that there is almost no numerical difference in u_{max} between the results obtained for W = 1648 m and for W = 4122 m. The small changes observed in u_{5m} and u_{10m} can be explained by the displacement of the convective cell in one case with respect to the other. To confirm this hypothesis, the convective cell centre is indicated with a black dot in Figure 13, and its coordinates (X_c, Y_c) are given in Table 8. When the valley width increases, the centre of the convective cell is displaced to the left (towards the mountain apex) and down (towards the near-slope area).

Table 8. Anabatic flow: maximum along-slope velocity (u_{max}) and along-slope velocity at a slope-normal distance of 5 m (u_{5m}) and 10 m (u_{10m}) at mid-slope for different valley widths (W) and coordinates of the convective cell centre (X_c, Y_c).

Parameter	W = 458 m	W = 1648 m	W = 4122 m
u_{max} [m/s]	−0.324	−0.346	−0.345
u_{5m} [m/s]	−0.217	−0.167	−0.178
u_{10m} [m/s]	−0.106	−0.062	−0.084
X_c [m]	331	301	284
Y_c [m]	1099	913	744

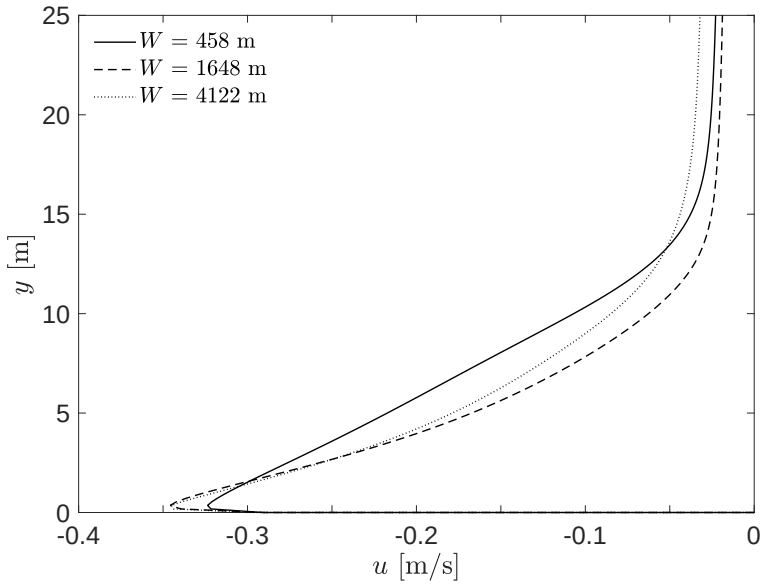

Figure 13. Anabatic flow: effect of valley width W on the along-slope velocity u vs. slope-normal distance y profile at mid-slope position for domain height $H = 2600$ m.

The same study is now repeated for the katabatic configuration. Figure 14 shows that the effect of the valley width on the velocity contours is a priori not very important. For the $W = 4122$ m case, for the sake of clarity, the figure only shows the field until $W = 1648$ m since the flow velocity is again virtually null on the right-hand side further away from the slope. We observe that once the width is large enough, no significant global differences are observed in the velocity contours though some local differences can be noted, especially in the transition zone from slope to flat area.

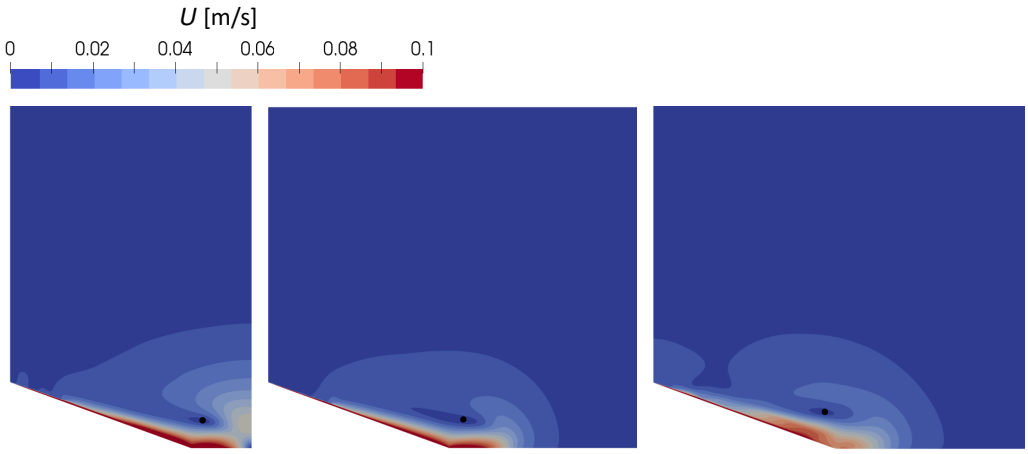

Figure 14. Katabatic flow: effect of valley width W on the velocity contours and cell generated over the slope (from left to right: $W = 458$, 1648, and 4122 m) for domain height $H = 2600$ m (the fluid domain with $X > 3022$ m over the flat valley is not shown for the right-hand side figure since velocity is close to zero in this area). The convective cell centre is indicated with a black dot.

The local flow behaviour at mid-slope is better appreciated in Figure 15, which shows the details of the velocity profile. It can be observed that as the valley width increases, the velocity profile gets closer to logarithmic (which would correspond to what has been reported for katabatic winds after experiments in [50] and after numerical analyses in [16,62] reaches a higher u_{max} (see Table 9)) and does not stabilise to a constant value as in the anabatic configuration. Again, the centre of the convective cell is indicated with a black dot in Figure 15, and its coordinates are given in Table 9. It can be seen that it does not

move much if comparing the results for $W = 458$ m and $W = 1648$ m; more specifically, it is located above the valley part, but moves upwards and towards the left (going back above the slope) when increasing W.

The effect of W can be regarded as limited when looking at the maximum velocity of the flow, especially in the anabatic case. For the katabatic one, the maximum velocity increases with W. Varying W also produces a displacement of the generated convective cell, which develops more above the slope in the anabatic case (and is located at lower heights as W increases) and more into the valley in the katabatic one (and is located at slightly higher heights as W increases). Future simulations of different valley widths should confirm these trends.

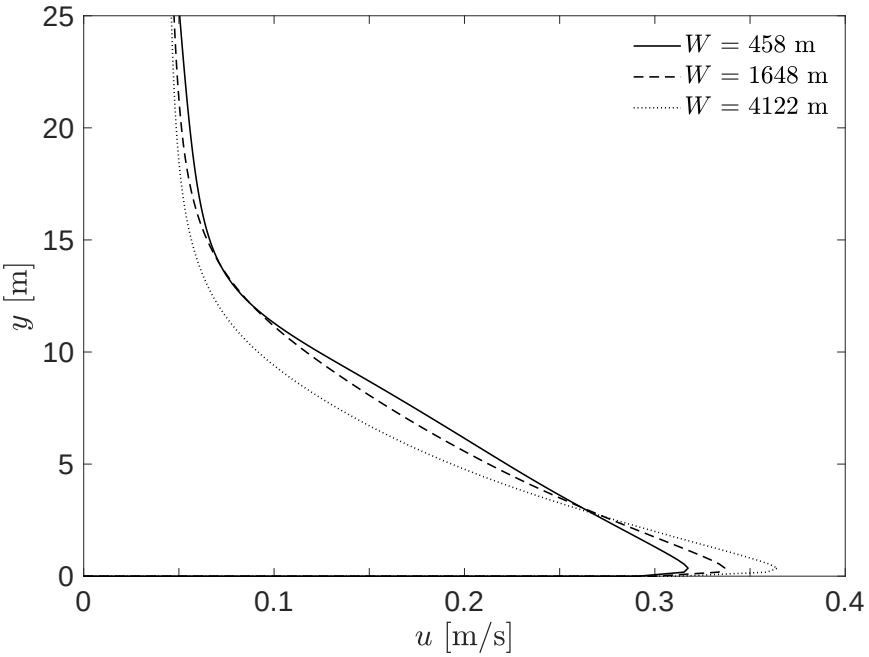

Figure 15. Katabatic flow: effect of valley width W on the along-slope velocity u vs. slope-normal distance y profile at mid-slope position for domain height $H = 2600$ m.

Table 9. Katabatic flow: maximum along-slope velocity (u_{max}) and along-slope velocity at a slope-normal distance of 5 m (u_{5m}) and 10 m (u_{10m}) at mid-slope for different valley widths (W) and coordinates of the convective cell centre (X_c, Y_c).

Parameter	$W = 458$ m	$W = 1648$ m	$W = 4122$ m
u_{max} [m/s]	0.3175	0.3368	0.3644
u_{5m} [m/s]	0.2217	0.2123	0.1928
u_{10m} [m/s]	0.1227	0.1163	0.0911
X_c [m]	1457	1491	1279
Y_c [m]	208	209	276

5. Conclusions

A new OpenFOAM setup has been proposed and tested to simulate the formation of slope winds. This research may be used to provide further insight on the structure and properties of these flows and for improving wind resource assessment in mountain–valley systems. To sum up, for simulations of mountain–valley thermally driven wind generation, the main conclusions of this work are the following:

- The use of temperature linearly dependent with altitude as a boundary condition for the slope is original and leads to a proper generation of slope thermally driven winds. Namely, the simulations correctly reproduce the flow acceleration and deceleration

observed along the slope: for the katabatic flow, the peak velocity increases as we move down the slope for the first half of the slope, and then drops in the second half of the slope, while in the anabatic flow, the peak velocity increases monotonically as we move up the slope. Moreover, the simulations correctly reproduce the trend of the slope-normal position of the peak velocity for the katabatic case.

- Numerical results are, as expected, very sensitive to the settings of field initial conditions. Imposing altitude-dependent temperature worsens the convergence of the simulation and is thus discarded.
- As a preliminary study of the influence of two RANS turbulence models, after comparison with LES results in the literature, the $k - \varepsilon$ model is found to be more suitable than the RNG $k - \varepsilon$ model.
- Similarly, the slip wall boundary condition on the top surface of the fluid domain is more adequate than a symmetry boundary condition, which leads to a much sharper near-wall velocity profile.
- As expected, the height of the computational domain greatly affects the field flow, and a minimum height to allow proper development of the convective cell in the flow field needs to be selected, and should be tested when changing the conditions of the simulations (slope angle, temperature gradient, etc.).
- Increasing the valley width does not significantly affect the magnitude of the thermally driven wind (especially in the anabatic case; in the katabatic one, the maximum velocity increases with the valley width). However, it does produce a displacement of the generated convective cell, which develops more above the slope in the anabatic case (and at lower height for a wider valley) and more into the valley in the katabatic one (and at higher height for a wider valley).

While one of the main objectives of this study was to increase the knowledge on how to use OpenFOAM for simulation of thermally driven winds, future work will focus on testing more possible models and assumptions, and on approaching more realistic simulations. Namely, it would be of interest to:

- Study more turbulence models and validate them against DNS results for thermally driven winds in idealised mountain–valley configurations.
- Study the effects of geometric parameters of the mountain–valley system (e.g., the slope angle) and of the initial flow velocity (since real mountain–valley flows have non-null initial velocity) and geostrophic velocity on the resulting wind speed profile, convective cell formation, etc.
- Perform a comparison of temperature and velocity profiles with experimental data obtained in similar conditions to the one described here in order to further validate the numerical simulations.
- Perform a complete 24 h cycle analysis. As a first step, a periodic time profile of the temperature boundary condition may be applied on the slope, maintaining all other assumptions equal to the ones described in this work. Then, the diurnal cycle can be studied, changing geometric parameters such as the slope angle.
- Study the effects of imposing some roughness on the slope and valley faces.

Future work thus aims at modelling more realistically mountain–valley regions to better estimate the peak speeds of thermally driven winds, to identify which parameters have the biggest effects on slope wind velocities and to contribute to improving the knowledge on assessment of the thermally driven wind resource in this kind of environment.

Author Contributions: Conceptualization, S.A., J.I.R. and A.M.; methodology, S.A., J.I.R. and A.M.; software, R.B.A.; validation, R.B.A.; formal analysis, S.A., J.I.R. and A.M.; investigation, all authors; resources, A.M.; data curation, S.A. and R.B.A.; writing—original draft preparation, J.I.R., R.B.A. and A.M.; writing—review and editing, S.A., J.I.R. and A.M.; visualization, S.A. and R.B.A.; supervision, J.I.R. and A.M.; project administration, A.M.; funding acquisition, S.A., J.I.R. and A.M. All authors have read and agreed to the published version of the manuscript.

Funding: This research was funded by AGAUR/*Generalitat de Catalunya*, with grant number 2017 SGR 1278, and by the Spanish Science and Innovation Ministry (MCIN) within the project TABL4CW, with grant number PID2019-105162RB-I00, funded by MCIN/AEI/10.13039/501100011033.

Institutional Review Board Statement: Not applicable.

Informed Consent Statement: Not applicable.

Data Availability Statement: Data available on demand.

Acknowledgments: We would like to thank the valuable feedback provided by Jordi Mazón.

Conflicts of Interest: The authors declare no conflict of interest. The funders had no role in the design of the study; in the collection, analyses, or interpretation of data; in the writing of the manuscript; or in the decision to publish the results.

Abbreviations

The following abbreviations are used in this manuscript:

ABL	atmospheric boundary layer
BC	boundary condition(s)
CFD	computational fluid dynamics
CFL	Courant-Friedrichs-Lewy
DES	detached-eddy simulations
DIC	diagonal incomplete-Cholesky
DILU	diagonal incomplete-LU
DNS	direct numerical simulations
HPC	High Performance Computing
IC	initial conditions(s)
LES	large-eddy simulations
PCG	preconditioned conjugate gradient
PBiCGStab	stabilised preconditioned (bi-) conjugate gradient
PIMPLE	PISO + SIMPLE
PISO	Pressure Implicit with Splitting of Operator
RANS	Reynolds-Averaged Navier–Stokes
RNG	Re-Normalisation Group
SIMPLE	Semi-Implicit Method for Pressure-Linked Equations
TKE	turbulence kinetic energy

References

1. Giometto, M.; Katul, G.; Fang, J.; Parlange, M. Direct numerical simulation of turbulent slope flows up to Grashof number $Gr = 2.1 \times 10^{11}$. *J. Fluid Mech.* **2017**, *829*, 589–620. [CrossRef]
2. Prandtl, L. *Führer Durch die Strömungslehre*; Vieweg und Sohn: Braunschweig, Germany, 1942; p. 382.
3. Stiperski, I.; Kavčič, I.; Grisogono, B.; Durran, D.R. Including Coriolis effects in the Prandtl model for katabatic flow. *Q. J. R. Meteorol. Soc.* **2007**, *133*, 101–106. [CrossRef]
4. Shapiro, A.; Fedorovich, E. Coriolis effects in homogeneous and inhomogeneous katabatic flows. *Q. J. R. Meteorol. Soc.* **2008**, *134*, 353–370. [CrossRef]
5. Zardi, D.; Serafin, S. An analytic solution for time-periodic thermally driven slope flows. *Q. J. R. Meteorol. Soc.* **2015**, *141*, 1968–1974. [CrossRef]
6. Giometto, M.; Grandi, R.; Fang, J.; Monkewitz, P.; Parlange, M. Katabatic flow: A closed-form solution with spatially varying eddy diffusivities. *Bound.-Layer Meteorol.* **2017**, *162*, 307–317. [CrossRef]
7. Shapiro, A.; Fedorovich, E. Katabatic flow along a differentially cooled sloping surface. *J. Fluid Mech.* **2007**, *571*, 149–175. [CrossRef]
8. Smith, C.M.; Skyllingstad, E.D. Numerical simulation of katabatic flow with changing slope angle. *Mon. Weather Rev.* **2005**, *133*, 3065–3080. [CrossRef]
9. Trachte, K.; Nauss, T.; Bendix, J. The impact of different terrain configurations on the formation and dynamics of katabatic flows: Idealised case studies. *Bound.-Layer Meteorol.* **2010**, *134*, 307–325. [CrossRef]
10. Egger, J. Thermally Forced Flows: Theory. In *Atmospheric Processes over Complex Terrain*; Blumen, W., Ed.; American Meteorological Society: Boston, MA, USA, 1990; Volume 23, pp. 43–58. ._3. [CrossRef]
11. Arduini, G.; Staquet, C.; Chemel, C. Interactions between the nighttime valley-wind system and a developing cold-air pool. *Bound.-Layer Meteorol.* **2016**, *161*, 49–72. [CrossRef]

12. Schumann, U. Large-eddy simulation of the up-slope boundary layer. *Q. J. R. Meteorol. Soc.* **1990**, *116*, 637–670. [CrossRef]
13. Skyllingstad, E.D. Large-eddy simulation of katabatic flows. *Bound.-Layer Meteorol.* **2003**, *106*, 217–243. [CrossRef]
14. Axelsen, S.; van Dop, H. Large-eddy simulation of katabatic winds. Part 1: Comparison with observations. *Acta Geophys.* **2009**, *57*, 803–836. [CrossRef]
15. Axelsen, S.; van Dop, H. Large-eddy simulation of katabatic winds. Part 2: Sensitivity study and comparison with analytical models. *Acta Geophys.* **2009**, *57*, 837–856. [CrossRef]
16. Brun, C.; Blein, S.; Chollet, J.P. Large-Eddy simulation of a katabatic jet along a convexly curved slope. Part I: Statistical results. *J. Atmos. Sci.* **2017**, *74*, 4047–4073. [CrossRef]
17. Umphrey, C.; DeLeon, R.; Senocak, I. Direct numerical simulation of turbulent katabatic slope flows with an immersed-boundary method. *Bound.-Layer Meteorol.* **2017**, *164*, 367–382. [CrossRef]
18. Berner, J.; Achatz, U.; Batté, L.; Bengtsson, L.; de la Cámara, A.; Christensen, H.M.; Colangeli, M.; Coleman, D.R.B.; Crommelin, D.; Dolaptchiev, S.I.; et al. Stochastic parameterization: Toward a new view of weather and climate models. *Bull. Am. Meteorol. Soc.* **2017**, *98*, 565–588. [CrossRef]
19. Duman, T.; Katul, G.G.; Siqueira, M.B.; Cassiani, M. A velocity-dissipation Lagrangian stochastic model for turbulent dispersion in atmospheric boundary-layer and canopy flows. *Bound.-Layer Meteorol.* **2014**, *152*, 1–18. [CrossRef]
20. Shirzadi, M.; Mirzaei, P.A.; Naghashzadegan, M. Improvement of k-epsilon turbulence model for CFD simulation of atmospheric boundary layer around a high-rise building using stochastic optimization and Monte Carlo Sampling technique. *J. Wind Eng. Ind. Aerodyn.* **2017**, *17*, 366–379. [CrossRef]
21. Wächter, M.; Heißelmann, H.; Hölling, M.; Morales, A.; Milan, P.; Mücke, T.; Peinke, J.; Reinke, N.; Rinn, P. The turbulent nature of the atmospheric boundary layer and its impact on the wind energy conversion process. *J. Turbul.* **2012**, *13*, N26. [CrossRef]
22. Muñoz-Esparza, D.; Kosović, B.; van Beeck, J.; Mirocha, J. A stochastic perturbation method to generate inflow turbulence in large-eddy simulation models: Application to neutrally stratified atmospheric boundary layers. *Phys. Fluids* **2015**, *27*, 035102. [CrossRef]
23. Cintolesi, C.; Mémin, E. Stochastic modelling of turbulent flows for numerical simulations. *Fluids* **2020**, *5*, 108. [CrossRef]
24. Yang, L.; Rojas, J.; Montlaur, A. Advanced methodology for wind resource assessment near hydroelectric dams in complex mountainous areas. *Energy* **2020**, *190*, 116487. [CrossRef]
25. Barcons, J.; Avila, M.; Folch, A. Diurnal cycle RANS simulations applied to wind resource assessment. *Wind Energy* **2019**, *22*, 269–282. [CrossRef]
26. Luo, Z.; Li, Y. Passive urban ventilation by combined buoyancy-driven slope flow and wall flow: Parametric CFD studies on idealized city models. *Atmos. Environ.* **2011**, *45*, 5946–5956. [CrossRef]
27. Chrust, M.; Whiteman, C.; Hoch, S. Observations of thermally driven wind jets at the exit of Weber Canyon, Utah. *J. Appl. Meteorol. Climatol.* **2013**, *52*, 1187–1200. [CrossRef]
28. Vihma, T.; Tuovinen, E.; Savijarvi, H. Interaction of katabatic winds and near-surface temperatures in the Antarctic. *J. Geophys. Res.* **2011**, *116*, D21119. [CrossRef]
29. Mazón, J.; Rojas, J.; Jou, J.; Valle, A.; Olmeda, D.; Sanchez, C. An assessment of the sea breeze energy potential using small wind turbines in peri-urban coastal areas. *J. Wind Eng. Ind. Aerodyn.* **2015**, *139*, 1–7. [CrossRef]
30. Dagdougui, H.; Minciardi, R.; Ouammi, A.; Robba, M.; Sacile, R. A dynamic decision model for the real-time control of hybrid renewable energy production systems. *IEEE Syst. J.* **2010**, *4*, 323–333. [CrossRef]
31. Cai, J.C.; Chen, H.J.; Brazhenko, V.; Gu, Y.H. Study of the Hydrodynamic Unsteady Flow Inside a Centrifugal Fan and Its Downstream Pipe Using Detached Eddy Simulation. *Sustainability* **2021**, *13*, 5113. [CrossRef]
32. Temel, O.; Bricteux, L.; van Beeck, J. Coupled WRF-OpenFOAM study of wind flow over complex terrain. *J. Wind Eng. Ind. Aerodyn.* **2018**, *174*, 152–169. [CrossRef]
33. Langheinrich, M.; Seifert, K. An Advanced Workflow for Simulating High Resolution Wind Fields Over Complex Urban Terrain Including Single Tree Objects. In Proceedings of the IGARSS 2019-2019 IEEE International Geoscience and Remote Sensing Symposium, Yokohama, Japan, 28 July–2 August 2019; pp. 7657–7660. [CrossRef]
34. Wang, L.; Su, J.; Gu, Z.; Shui, Q. Effect of Street Canyon Shape and Tree Layout on Pollutant Diffusion under Real Tree Model. *Sustainability* **2020**, *12*, 2105. [CrossRef]
35. Churchfield, M.; Moriarty, P.; Vijayakumar, G.; Brasseur, J. Wind Energy-Related Atmospheric Boundary Layer Large-Eddy Simulation Using OpenFOAM. In Proceedings of the 19th Symposium on Boundary Layers and Turbulence, Keystone, CO, USA, 2–6 August 2010. Available online: https://www.nrel.gov/docs/fy10osti/48905.pdf (accessed on 8 January 2023).
36. Chaudhari, A.; Vuorinen, V.; Agafonova, O.; Hellsten, A.; Hämäläinen, J. Large eddy simulations for atmospheric boundary layer flows over complex terrains with applications in wind energy. In Proceedings of the 11th World Congress on Computational Mechanics, Barcelona, Spain, 20–25 July 2014.
37. Cintolesi, C.; Di Santo, D.; Barbano, F.; Di Sabatino, S. Anabatic Flow along a Uniformly Heated Slope Studied through Large-Eddy Simulation. *Atmosphere* **2021**, *12*, 850. [CrossRef]
38. Fedorovich, E.; Shapiro, A. Structure of numerically simulated katabatic and anabatic flows along steep slopes. *Acta Geophys.* **2009**, *57*, 981–1010. [CrossRef]
39. Heinemann, G.; Klein, T. Modelling and observations of the katabatic flow dynamics over Greenland. *Tellus A* **2002**, *54*, 542–554. [CrossRef]

40. Renfrew, I. The dynamics of idealized katabatic flow over a moderate slope and ice shelf. *Q. J. R. Meteorol. Soc.* **2004**, *130*, 1023–1045. [CrossRef]
41. Shapiro, A.; Burkholder, B.; Fedorovich, E. Analytical and numerical investigation of two-dimensional katabatic flow resulting from local surface cooling. *Bound.-Layer Meteorol.* **2012**, *145*, 249–272. [CrossRef]
42. OpenFOAM v7 User Guide. Available online: https://cfd.direct/openfoam/user-guide (accessed on 15 September 2022).
43. Bechmann, A. Large-Eddy Simulation of Atmospheric Flow over Complex Terrain. Ph.D Thesis, Riso National Laboratory, Technical University of Demnark, Roskilde, Demnark, 2006.
44. Senocak, I.; Ackerman, A.; Kirkpatrick, M.; Stevens, D.; Mansour, N. Study of near-surface models for large-eddy simulations of a neutrally stratified atmospheric boundary layer. *Bound.-Layer Meteorol.* **2007**, *124*, 405–424. [CrossRef]
45. Liu, F. A thorough description of how wall functions are implemented in OpenFOAM. In *Proceedings of CFD with OpenSource Software*; Nilsson, H., Ed.; Chalmers University of Technology: Gothenburg, Sweden, 2016
46. Yan, B.; Li, Q. Coupled on-site measurement/CFD based approach for high-resolution wind resource assessment over complex terrains. *Energy Convers. Manag.* **2016**, *117*, 351–366. [CrossRef]
47. Mochida, A.; Lun, I.Y. Prediction of wind environment and thermal comfort at pedestrian level in urban area. *J. Wind Eng. Ind. Aerodyn.* **2008**, *96*, 1498–1527. [CrossRef]
48. Hargreaves, D.; Wright, N. On the use of the k-ε model in commercial CFD software to model the neutral atmospheric boundary layer. *J. Wind Eng. Ind. Aerodyn.* **2007**, *95*, 355–369. [CrossRef]
49. OpenFOAM: API Guide v2112. The Open Source CFD Toolbox. Available online: https://www.openfoam.com/documentation/guides/latest/api/index.html (accessed on 15 September 2022).
50. Charrondière, C.; Brun, C.; Cohard, J.M.; Sicart, J.E.; Obligado, M.; Biron, R.; Coulaud, C.; Guyard, H. Katabatic winds over steep slopes: Overview of a field experiment designed to investigate slope-normal velocity and near-surface turbulence. *Bound.-Layer Meteorol.* **2022**, *182*, 29–54. [CrossRef]
51. Foken, T. Decoupling between the atmosphere and the underlying surface during stable stratification. *Bound.-Layer Meteorol.* **2022**. [CrossRef]
52. Versteeg, H.K.; Malalasekera, W. *An Introduction to Computational Fluid Dynamics: The Finite Volume Method*, 2nd ed.; Pearson Education Ltd.-Prentice Hall: Harlow, UK, 2007; p. 503.
53. Hewitt, R.; Unadkat, J.; Wise, A. Shallow katabatic flow on a non-uniformly cooled slope. *Environ. Fluid Mech.* **2022**. [CrossRef]
54. Shapiro, A.; Fedorovich, E. A boundary-layer scaling for turbulent katabatic flow. *Bound.-Layer Meteorol.* **2014**, *153*, 1–17. [CrossRef]
55. Alards, K.; Kunnen, R.; Stevens, R.M.; Lohse, D.; Toschi, F.; Clercx, H. Sharp transitions in rotating turbulent convection: Lagrangian acceleration statistics reveal a second critical Rossby number. *Phys. Rev. Fluids* **2019**, *4*, 074601. [CrossRef]
56. Kenjeres, S. Heat transfer enhancement induced by wall inclination in turbulent thermal convection. *Phys. Rev. E* **2015**, *92*, 053006. [CrossRef]
57. Catalano, F.; Moeng, C. Large-eddy simulation of the daytime boundary layer in an idealized valley using the Weather Research and Forecasting numerical model. *Bound.-Layer Meteorol.* **2010**, *137*, 49–75. [CrossRef]
58. Launder, B.E.; Spalding, D.B. The numerical computation of turbulent flows. *Comput. Methods Appl. Mech. Eng.* **1974**, *3*, 269–289. [CrossRef]
59. Franke, J.; Hellsten, A.; Schlünzen, H.; Carissimo, B. Best Practice Guideline for the CFD Simulation of Flows in the Urban Environment. In Proceedings of the 11th Conference on Harmonisation within Atmospheric Dispersion Modelling for Regulatory Purposes, Cambridge, UK, 2–5 July 2007; p. 52.
60. Grisogono, B.; Oerlemans, J. A theory for the estimation of surface fluxes in simple katabatic flows. *Q. J. R. Meteorol. Soc.* **2001**, *127*, 2725–2739. [CrossRef]
61. Simpson, J.E. *Sea Breeze and Local Winds*; Cambridge University Press: Cambridge, UK, 1994; p. 234.
62. Bautista, M.C. Turbulence Modelling of the Atmospheric Boundary Layer over Complex Topography. Ph.D Thesis, Université de Québec, École de Technologie Supérieure, Québec, QC, Canada, 2015.